

Optics-Free, Non-Contact Measurements of Fluids, Bubbles, and Particles in Microchannels Using Metallic Nano-Islands on Graphene

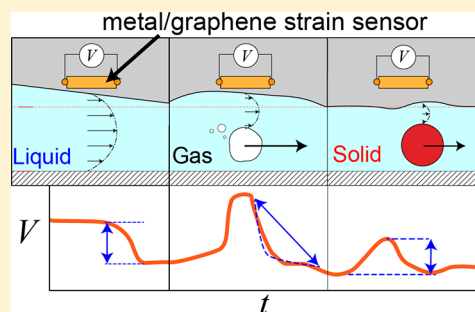
Charles Dhong, Samuel J. Edmunds, Julian Ramírez, Laure V. Kayser, Fang Chen,^{1b} Jesse V. Jokerst, and Darren J. Lipomi*^{1b}

Department of NanoEngineering, University of California, San Diego, 9500 Gilman Drive, Mail Code 0448, La Jolla, California 92093, United States

Supporting Information

ABSTRACT: Despite the apparent convenience of microfluidic technologies for applications in healthcare, such devices often rely on capital-intensive optics and other peripheral equipment that limit throughput. Here, we monitored the transit of fluids, gases, particles, and cells as they flowed through a microfluidic channel without the use of a camera or laser, i.e., “optics-free” microfluidics. We did this by monitoring the deformation of the side walls caused by the analyte passing through the channel. Critically, the analyte did not have to make contact with the channel walls to induce a deflection. This minute deformation was transduced into a change in electrical resistance using an ultrasensitive piezoresistive film composed of metallic nano-islands on graphene. We related changes in the resistance of the sensor to the theoretical deformation of the channel at varying flow rates. Then, we used air bubbles to induce a perturbation on the elastomeric channel walls and measured the viscoelastic relaxation of the walls of the channel. We obtained a viscoelastic time constant of $11.3 \pm 3.5 \text{ s}^{-1}$ for polydimethylsiloxane, which is consistent with values obtained using other techniques. Finally, we flowed silica particles and human mesenchymal stem cells and measured the deformation profiles of the channel. This technique yielded a convenient, continuous, and non-contact measurement of rigid and deformable particles without the use of a laser or camera.

KEYWORDS: Strain sensor, graphene, viscous fluids, elastohydrodynamics, particles, bubbles



Microfluidic devices have long been touted as a powerful analytical tool with which to characterize a wide range of analytes, including particles, cells, and fluids.^{1–5} These devices, however, have not seen wide-scale adoption outside of the laboratory³ because they require significant capital. An individual microfluidic device might not be expensive, but the vast majority⁶ of microfluidic devices operate using optics-based principles, which typically require high-speed or sensitive cameras, sophisticated confocal microscopes, vibration isolation tables, and laser excitation systems, which often require fluorescent probes.^{7–9} We describe a novel technique that does not rely on the optical-based characterization of fluid flow and analytes.

We embedded thin-film strain sensors made from palladium nano-islands deposited on single-layer graphene¹⁰ in the bulk of the elastomer in close proximity to a channel wall. The composite film measures changes in the electrical resistance caused by deformation of the wall (Figure 1a). This deformation can be related to the fluid flow¹¹ or to the properties of a flowing particle.^{12,13} The couplings that occur between fluid flow and elastic structures are known as elastohydrodynamic phenomena.^{11,14–16} In addition to measuring analytes, the platform we describe could be used to validate elastohydrodynamic theories, which can be difficult with current experimental techniques.^{17,18} In contrast with

other methods of measuring and sorting objects in microfluidic channels, this method does not place an obstacle in the pathway of an analyte. Some of the current techniques of mechanical sensing require analytes to be flowed over cantilevers^{19,20} or around mechanical features,^{21,22} such as spirals. Cantilever measurements, however, still require lasers to capture small deflections of the tip and must be rigorously isolated from vibration. Differentiating analytes based on mechanical features, either through biasing flow around features (e.g., deformability-based cell margination)^{23–25} or through collisions into obstacles (e.g., deterministic lateral displacement),²⁶ can be limited in throughput by the speed of the camera used for sorting and damage caused to the structures or to the analyte.

To transduce the deformation of the walls that occurs on the micron scale (Figure 1b), we found it advantageous to use sensors that did not need to be placed in the fluid environment. We fabricated a composite metal-on-graphene piezoresistive sensor, previously developed in our laboratory, by evaporating palladium onto single-layer graphene (Figure 1d). These sensors can measure strains as low as 0.001%.^{10,27}

Received: June 6, 2018

Revised: July 16, 2018

Published: July 19, 2018

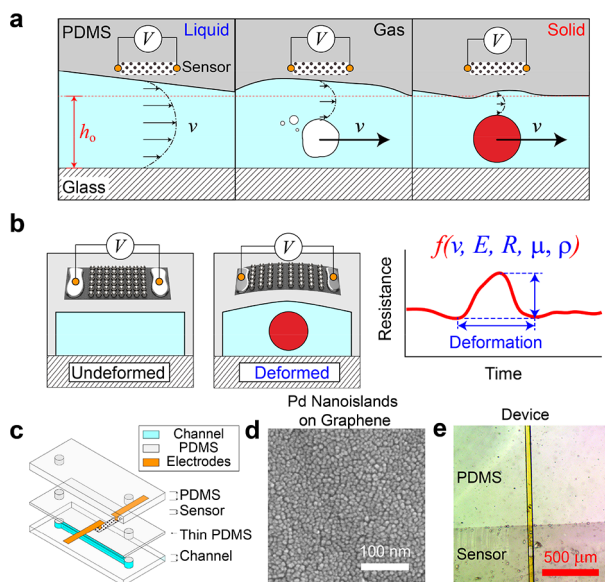


Figure 1. (a) Fluid flowing against a soft wall, such as poly-(dimethylsiloxane) (PDMS), deforms the channel in relation to the fluid flow rate (v) and viscosity. Air bubbles and solid particles also cause distinctive deformation profiles along the channel wall. (b) Piezoresistive thin films composed of palladium nano-islands on graphene placed near the channel can transduce minute elastohydrodynamic deformation into voltage changes. (c) Schematic diagram of the device showing placement of the sensor near the channel. (d) Scanning electron microscope (SEM) images of palladium nano-islands on graphene. (e), Bright-field image of device with the edge of the sensor and fluid channel visible.

The sensitivity at low strains is attributed to a combination of phenomena, including strain-induced scattering between nano-islands initially in contact and modulation of the tunneling current between metallic nano-islands once separated, along with the intrinsic piezoresistance of graphene.¹⁰ While there are other strain sensors with high gauge factors,^{28,29} we required high sensitivity at low strains, minimal fabrication steps, low physical profiles, and ultralow stiffness so as to have a negligible effect on the mechanical response of the sidewalls of the channels. We fabricated simple microfluidic devices out of poly(dimethylsiloxane) (PDMS) containing a single, straight channel, with the strain sensor embedded near the channel (Figure 1c–e). Devices differed in their cross-sectional dimensions (width \times height) as well as by the Young's modulus of the PDMS (achieved by varying the base-to-cross-linker ratio). Full details of fabrication can be found in the Supporting Information.

We connected the microfluidic devices to a commercial PID-controlled, isocratic fluid pump (1260 Infinity II GPC/SEC, Agilent) and measured the changes in resistance of the sensor at different flow rates of water for different devices. The raw data can be seen in Figure 2a,b, which were taken with the device directly on a bench without isolation from vibration. Most ultra-sensitive sensors suffer from unwanted detection of ambient vibration. Embedding the sensor in the viscoelastic elastomer dampened these ambient vibrations, which enabled the sensor to measure the submicron deformations in the channel with a signal well above the background mechanical noise.

A change of 0.1% in resistance during flow rate measurements corresponds to increments of absolute resistance on the

order of $10\ \Omega$. Given a flow rate, we can relate the imposed channel deformation by a fluid using the relationships developed by Gervais et al.¹¹ (used here) or Christov et al.³⁰ The channel deformation is (and shown in Figure 2c):

$$Q = \frac{h_0^4 E}{48\alpha\mu(L - z_{\text{sensor}})} \left(\left(1 + \frac{\alpha p(z)W}{Eh_0} \right)^4 - 1 \right) \quad (1)$$

$$\frac{\Delta h}{h_0} = 2\sqrt{\frac{3Q\mu(L - z_{\text{sensor}})}{h_0^4 E} + 1} - 1 \quad (2)$$

where Q is the flow rate, h_0 is the initial channel height, E is the elastic modulus of the channel walls in the device, L is the length of the channel, z is the axial position along the device, μ is the fluid viscosity, W is the width of the channel, $p(z)$ is the pressure distribution along the channel, and α is a proportionality constant with a range from 0.5 to 15^{31} (see refs 30 and 31 and the Supporting Information for more details). For high pressures, such as in the device with a relatively small $50 \times 50\ \mu\text{m}$ cross-sectional area, the relationship between deformation and flow rate became noticeably nonlinear. Thus, in Figure 2d, the relationship between changes in resistance and deformation are linear for the three devices with a larger cross-sectional area but not the $50\ \mu\text{m} \times 50\ \mu\text{m}$ device (red diamonds). We obtained a normalized change in resistance, which normalizes the sensitivity of the nano-islands on graphene sensor and the distance of the sensor from the fluid channel, by multiplying the change slope, m , compared to a reference slope, m_0 , of the device with dimensions $750\ \mu\text{m} \times 200\ \mu\text{m}$, $E = 2\ \text{MPa}$. This value, m/m_0 , is denoted as the “gain” in Figure 2e. On the y axis, we have plotted the normalized change in resistance of the palladium nano-island strain sensor, which is proportional to the strain. On the x axis, we have plotted our experimental conditions in the form of $\Delta h/h_0$, which relates the strain in the channel assuming elastohydrodynamic deformation, given by eq 2. We observed a collapse of the data in the linear regime onto a single master plot with a slope of 0.78, which is in close agreement to a theoretical value of 1. This demonstrates that the sensor is sensing deformation due to elastohydrodynamic phenomenon. The deviation from the theoretical value could be due to differences between the devices and theory:¹¹ the devices here do not have a limiting dimension, and for the purposes of demonstrating trends in strain with flow rate, we have simply taken the fitting parameter, α , to be 1. In addition, the distance between the sensor to the channel can vary between devices ($\sim 1\text{--}3\ \mu\text{m}$), which decreases the strain as the sensor is further in the bulk (the strain on the sensor, however, remains proportional to the deformation on the sidewalls).³² Christov et al. solved for α without requiring simulations, but this approach had a thin, deformable layer on top of the channel, whereas the devices here have a semi-infinite layer on top.³⁰

We measured the transient changes in channel deformation due to air bubbles ($\sim 30\text{--}50\ \mu\text{L}$) in a device with cross-sectional dimensions of $300\ \mu\text{m} \times 300\ \mu\text{m}$, made with PDMS with a modulus of $1\ \text{MPa}$. In contrast to previous studies that used optical methods,^{33,34} we were able to monitor dynamic events in the channel at far higher rates ($\sim 10\ \text{kHz}$ sampling rates) that accessible to most cameras ($\sim 20\text{--}100\ \text{Hz}$) and without optical limits (micron-or-less wall deformation). Figure 3a shows the relatively large changes in resistance as

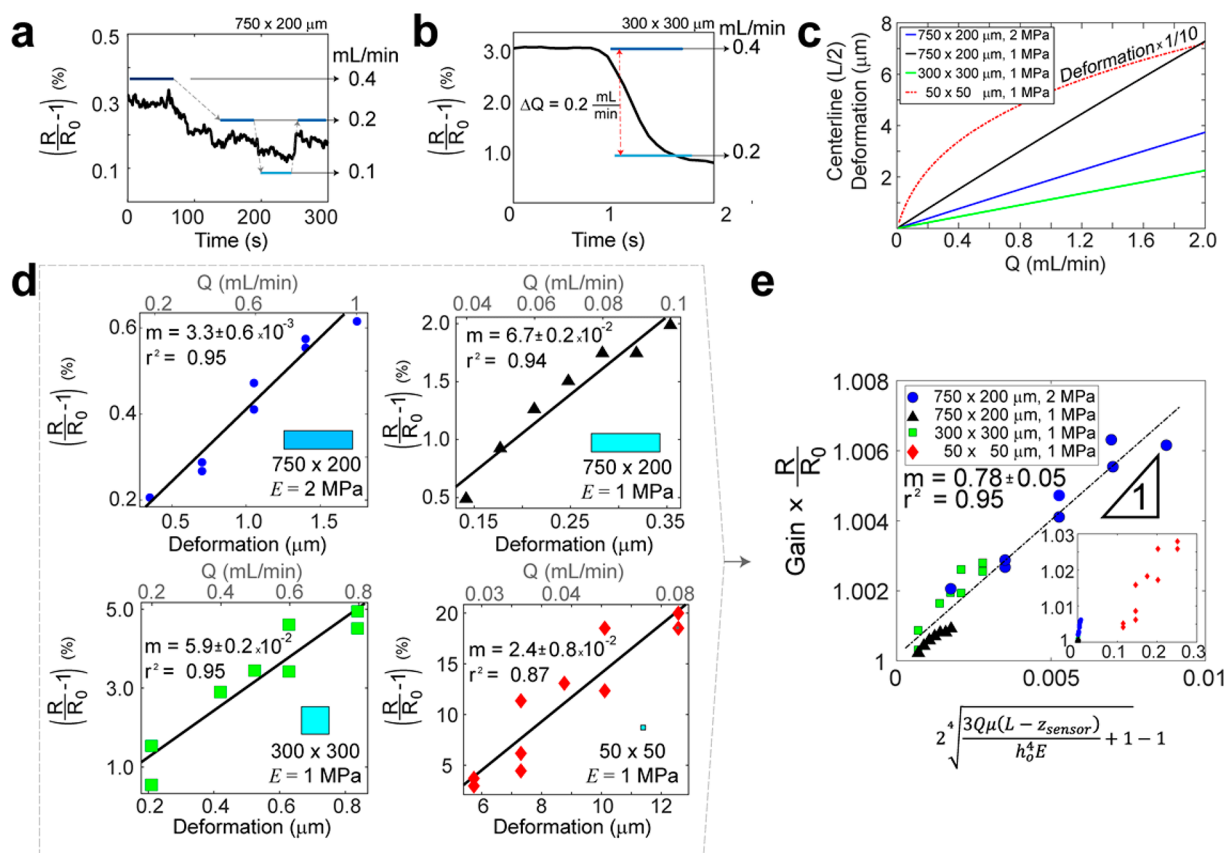


Figure 2. (a) Recording resistance changes in the device due to changes in flow rate (right y-axis) into the device. (b) Changes in resistance quickly followed changes in the flow rate. (c) Theoretical relationship between fluid flow rate and channel deformation for devices tested here, calculated according to ref 11. Note the 1/10 factor on the $50 \times 50 \mu\text{m}$ device (red dashed line). (d) Percent change in resistance at different flow rates, plotted against the theoretical deformation at the wall for several devices in varying geometries and elastic modulus. Gain and linearity given by slope and r^2 values, respectively. (e) Master curve relating channel deformation to changes in resistance for all devices. Naming convention are the channel's width (W) by the channel's height (H) in microns, followed by the elastic modulus of the device. Error of slope calculated on confidence intervals of 95%.

a bubble flowed past the sensor, with variations due to velocity and size of bubbles. The large change in resistance is surprising because the pressure drop across a $30\text{--}50 \mu\text{L}$ bubble is small: approximately $\sim 5\text{--}50 \text{ Pa}$ for flow velocities of 1 to 10 mm/s.³⁵ To investigate the origin of these large changes in resistance, we measured the resistance while taking high-speed video (Basler Ace, 820 FPS) for the case of an “infinitely-long” bubble, where a channel of fluid is cleared by air. Figure 3b shows the calculated deformation due to a transiting “infinitely long” bubble. We show the sensor resistance and deformation (micrometers) on the other y axis, as calculated from the fluid flow rate, by dividing the percent relative change in resistance ($R_0 = 5.35 \text{ k}\Omega$) by $5.9 \times 10^{-2} \text{ m}$ (Figure 2d). By doing so, we assumed that the deformation profile over the strain sensor was the same between a pure fluid and an air bubble; they presumably deform the walls with a different profile, but the magnitude of deformation on the sensor is similar.

In region 0, the channel was flowing with only water; we applied a small increase in flow rate, indicated by the green arrow, to serve as a calibration. This pulse highlights the magnitude of the signals produced by air bubbles compared with those produced by changes in flow rate. In region I, we observed that the resistance began to increase rapidly; from the image in Figure 3c, we determined that this increase corresponds to the air–water interface transiting across the sensor. In region II, the image from Figure 3d shows that the

fluid interface has passed the sensor, which corresponds to the lengthy plateau in the normalized resistance in Figure 3b. This plateau, which has a modest negative linear slope, corresponds to clearing of the channel of fluid with air because the sensor was located in the middle of the channel. We have observed that clearing the channel with air at higher velocities results in a shorter plateau and vice versa. This process was mechanically noisy as the channel sputtered water, which is reflected in the deformation trace in Figure 3d.

We took advantage of this phenomenon to measure the viscoelasticity of the PDMS. Figure 3e shows the channel relaxing in the absence of any fluid. Using a Kelvin–Voigt model of viscoelastic materials,³⁶ the transient change in resistance (normalized by maximum resistance) was treated as a spring dashpot (dashed lines, Figure 3f). This spring dashpot responded to the changes in fluid within the channel, represented as a square wave with a width that spans region I to region II. We obtained a viscoelastic relaxation time constant, τ , of $11.3 \pm 3.5 \text{ s}^{-1}$ and viscosity (of the solid) of $0.20 \pm 0.08 \text{ MPa}\cdot\text{s}$, which compares reasonably well to 7.2 s^{-1} and $0.15 \text{ MPa}\cdot\text{s}$, in the literature (hexane-extracted 10:1 PDMS measured with an elastic modulus of 1.08 MPa).¹⁷ The maximum frequency of bubbles we achieved was at 33 Hz (see Figure S4) and was limited by our capability to generate bubbles rapidly. This rate could potentially be increased because the maximum frequency was limited by our ability to

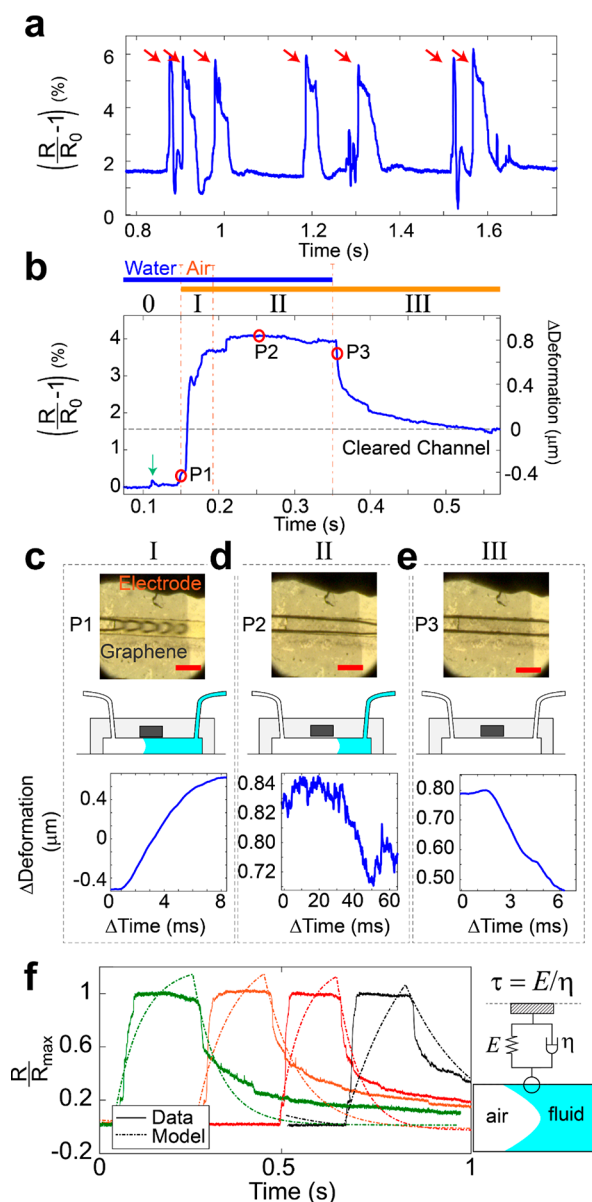


Figure 3. Detecting air bubbles and measuring viscoelasticity of the channel. (a) Flowing 30–50 μL air bubbles in water causes large changes in resistance in the device made of $E = 1$ MPa PDMS with channel dimensions of $300\ \mu\text{m} \times 300\ \mu\text{m}$. Air bubbles are indicated with red arrows. (b) Clearing the channel with air creates several identifiable regions from 0–III. The green arrow indicates a calibration peak. The baseline with zero corresponded to the deformation of the open channel. (c) Region I, in which the air bubble began to transit under the sensor. Micrograph from the video (top, 820 FPS), a schematic drawing of fluid (middle), and deformation of the wall (bottom). (d) Region II, in which the air bubble displaces water completely from channel under the sensor. (e) Region III, in which the channel was void of fluid but the wall deformation occurred over some finite domain due to viscoelastic relaxation. Deformation calculated from fluid calibration. (f) Kelvin–Voigt model of viscoelastic relaxation of several trials in channel walls (dashed lines) as compared with the data (solid lines). Scale bar: 1 mm in the micrographs P1–P3.

generate bubbles, rather than to the mechanical response of the material.

We have confirmed that large changes in resistance occur when the air–water interface moves across the channel. The

strain profile caused by a moving air–water interface is unusual: most strain sensors experience a gradual change in deflection across the majority of the sensor, e.g., a strain sensor bent like a cantilever. We hypothesize that large changes in the resistance of the sensor, through the PDMS side walls, occur due to relatively high compression (i.e., strain) in a narrow portion, around the air–water interface, as opposed to a gradual bend across the length of the entire sensor.

We then examined the deformation of rigid particles (silica microspheres) and deformable objects (human mesenchymal stem cells) as they transited through the channel. As a particle transits through a channel, it causes the fluid to flow around the particle, deforming the walls of the channel.^{13,18,37} The silica spheres (Megabead, PolySciences, Inc., calibration grade, $\text{CV} < 3\%$) were $80\ \mu\text{m}$ in diameter and flowed through a device with cross-sectional dimensions of $300\ \mu\text{m} \times 300\ \mu\text{m}$, made with PDMS ($E = 1$ MPa). Figure 4a shows the change in

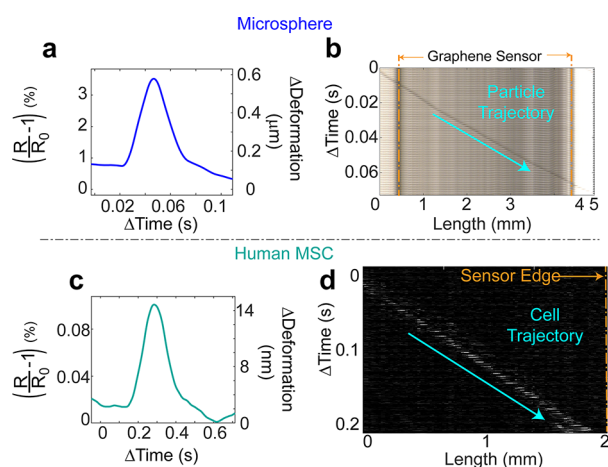


Figure 4. Deformation profiles of silica particles and human mesenchymal stem cells. (a) $80\ \mu\text{m}$ silica particles were flown through a $300\ \mu\text{m} \times 300\ \mu\text{m}$, $E = 1$ MPa channel, causing resistance changes. These resistance changes were converted to channel deformation per calibration from Figure 2. In panel b, portions of images taken as particle passed through fluidic channel and over the sensor, delineated in orange. (c) Human mesenchymal stem cells ($25\text{--}40\ \mu\text{m}$ in diameter) were flown in the same channel geometry, and the channel deformation was monitored. In panel d, portions of image as cells passed through the fluidic channel. The background image was subtracted to highlight cell motion with the cyan line to guide the eye. Metal nano-island-on-graphene sensor interface is shown with an orange dashed line.

resistance and the calculated change in deformation as the silica sphere flowed past the sensor. Again, this assumes that the deformation caused by the particle and a pure fluid is the same, which is not necessarily true but gives a magnitude of channel deformation. A sequence of images showing the silica sphere past the sensor can be seen in Figure 4b.

We see that the change in resistance (Figure 4a) of the sphere follows a linear increase as the particle transits across the sensor, reaching a maximum after approximately 30 ms. At this moment (Figure 4b), the particle was approximately $2/3$ of the way through the sensor (at a length of 2.8 mm). It is not immediately clear why the maximum resistance was a sharp peak, but the presence of a peak suggests that the particle deforms the walls in front and behind the actual particle.

Human-derived mesenchymal stem cells (hMSCs, Lonza, PT-2501) were trypsinized and then flown into the device to

demonstrate a proof-of-principle in measuring the deformability of the side walls due to the transit of biological objects in a continuous manner. This capability could be advantageous in the high-throughput screening of cells that differ in mechanical properties only, such as the label-free detection of circulating tumor cells.³⁸ Cells were approximately 25–40 μm in diameter, and the resistance and deformation on the sensor caused by a cell flowing in the 300 μm \times 300 μm device is shown in Figure 4c. The cell is both smaller and softer than the silica particle, and we see a smaller signal from the sensor. A composite image of the cell motion in a channel is shown in Figure 4d. The velocity of the moving particle, whether cell or silica sphere, affects the amount of deformation on the wall, and particles that move too slowly will not be detectable. Future development of the theoretical elastohydrodynamic deformation profile may make it simpler to distinguish between air bubbles, rigid particles, and cells from the characteristic time-dependent resistance recorded by the sensor during transit of the object.

We demonstrated that the deformation of the sidewalls in a microfluidic channel could be used to measure a variety of phenomenon, such as the fluid flow rates, the viscoelastic relaxation of the channel side walls in the presence of air bubbles, and channel deformation caused by particles and cells. This technique may enable new avenues of investigation in physics and biology. These devices can be used to experimentally verify novel elastohydrodynamic phenomenon, such as the passage of deformable particles in the presence of deformable walls, or the flow around a deformable junction in the channel. Within cell biology, this device is complementary to many existing optical techniques because it only requires that one of the channel walls is deformable. For example, this device could provide a method of continuously measuring the mechanical properties of cells.

■ ASSOCIATED CONTENT

■ Supporting Information

The Supporting Information is available free of charge on the ACS Publications website at DOI: 10.1021/acs.nanolett.8b02292.

Additional experimental details, channel deformation, and maximum frequency for detecting bubbles. Figures showing bright-field microscopy, schematics of channel geometry and variables, calculated channel deformation, voltage signals, and expansion of the time window. A table showing model parameters. (PDF)

■ AUTHOR INFORMATION

Corresponding Author

*E-mail: dlipomi@eng.ucsd.edu.

ORCID

Fang Chen: 0000-0002-6675-5508

Darren J. Lipomi: 0000-0002-5808-7765

Notes

The authors declare the following competing financial interest(s): D.J.L. is an inventor on a patent related to the use of metallic nano-islands on graphene as a means of mechanical sensing and is a shareholder in GrollTex, Inc., which supplied the graphene used in this study.

■ ACKNOWLEDGMENTS

We acknowledge financial support through the NIH Director's New Innovator Award, grant no. 1DP2EB022358-03. to D.J.L. Additionally, J.R. acknowledges support provided by the NSF Graduate Research Fellowship Program under grant no. DGE-1144086. F.C. and J.V.J. acknowledge support from the NIH (DP2 HL137187 and R01 HL 117048)

■ REFERENCES

- (1) Wyatt Shields, C., IV; Reyes, C. D.; López, G. P. Microfluidic cell sorting: a review of the advances in the separation of cells from debulking to rare cell isolation. *Lab Chip* **2015**, *15* (5), 1230–1249.
- (2) Sackmann, E. K.; Fulton, A. L.; Beebe, D. J. The present and future role of microfluidics in biomedical research. *Nature* **2014**, *507* (7491), 181–9.
- (3) Blow, N. Microfluidics: in search of a killer application. *Nat. Methods* **2007**, *4* (8), 665–668.
- (4) Sant, S.; Tao, S. L.; Fisher, O. Z.; Xu, Q.; Peppas, N. A.; Khademhosseini, A. Microfabrication technologies for oral drug delivery. *Adv. Drug Delivery Rev.* **2012**, *64* (6), 496–507.
- (5) Hashimoto, M.; Tong, R.; Kohane, D. S. Microdevices for nanomedicine. *Mol. Pharmaceutics* **2013**, *10* (6), 2127–44.
- (6) Tamayo, J.; Kosaka, P. M.; Ruz, J. J.; San Paulo, A.; Calleja, M. Biosensors based on nanomechanical systems. *Chem. Soc. Rev.* **2013**, *42* (3), 1287–311.
- (7) Kuswandi, B.; Huskens, J.; Verboom, W.; Nuriman. Optical sensing systems for microfluidic devices: a review. *Anal. Chim. Acta* **2007**, *601* (2), 141–155.
- (8) Andersson, H.; van den Berg, A. Microfluidic devices for cellomics: a review. *Sensors and Actuators B. Sens. Actuators, B* **2003**, *92* (3), 315–325.
- (9) Pfeiffer, S. A.; Nagl, S. Microfluidic platforms employing integrated fluorescent or luminescent chemical sensors: a review of methods, scope and applications. *Methods Appl. Fluoresc.* **2015**, *3* (3), 034003.
- (10) Zaretski, A. V.; Root, S. E.; Savchenko, A.; Molokanova, E.; Printz, A. D.; Jibril, L.; Arya, G.; Mercola, M.; Lipomi, D. J. Metallic Nanoislands on Graphene as Highly Sensitive Transducers of Mechanical, Biological, and Optical Signals. *Nano Lett.* **2016**, *16* (2), 1375–1380.
- (11) Gervais, T.; El-Ali, J.; Gunther, A.; Jensen, K. F. Flow-induced deformation of shallow microfluidic channels. *Lab Chip* **2006**, *6* (4), 500–7.
- (12) Rallabandi, B.; Saintyves, B.; Jules, T.; Salez, T.; Schonecker, C.; Mahadevan, L.; Stone, H. A. Rotation of an immersed cylinder sliding near a thin elastic coating. *Phys. Rev. Fluids* **2017**, *2* (7), 074102.
- (13) Urzay, J.; Llewellyn Smith, S. G.; Glover, B. J. The elastohydrodynamic force on a sphere near a soft wall. *Phys. Fluids* **2007**, *19* (10), 103106.
- (14) Leroy, S.; Steinberger, A.; Cottin-Bizonne, C.; Restagno, F.; Leger, L.; Charlaix, E. Hydrodynamic interaction between a spherical particle and an elastic surface: a gentle probe for soft thin Films. *Phys. Rev. Lett.* **2012**, *108* (26), 264501.
- (15) Wang, Y. M.; Dhong, C.; Frechette, J. Out-of-Contact Elastohydrodynamic Deformation due to Lubrication Forces. *Phys. Rev. Lett.* **2015**, *115* (24), 248302.
- (16) Dhong, C.; Frechette, J. Peeling flexible beams in viscous fluids: Rigidity and extensional compliance. *J. Appl. Phys.* **2017**, *121* (4), 044906.
- (17) Wang, Y. M.; Pilkington, G. A.; Dhong, C.; Frechette, J. Elastic deformation during dynamic force measurements in viscous fluids. *Curr. Opin. Colloid Interface Sci.* **2017**, *27*, 43–49.
- (18) Pandey, A.; Karpitschka, S.; Venner, C. H.; Snoeijer, J. H. Lubrication of soft viscoelastic solids. *J. Fluid Mech.* **2016**, *799*, 433–447.
- (19) Kartanas, T.; Ostanin, V.; Challa, P. K.; Daly, R.; Charmet, J.; Knowles, T. P. J. Enhanced Quality Factor Label-free Biosensing with

Micro-Cantilevers Integrated into Microfluidic Systems. *Anal. Chem.* **2017**, 89 (22), 11929–11936.

(20) Bircher, B. A.; Duempelmann, L.; Renggli, K.; Lang, H. P.; Gerber, C.; Bruns, N.; Braun, T. Real-time viscosity and mass density sensors requiring microliter sample volume based on nanomechanical resonators. *Anal. Chem.* **2013**, 85 (18), 8676–83.

(21) Darling, E. M.; Di Carlo, D. High-Throughput Assessment of Cellular Mechanical Properties. *Annu. Rev. Biomed. Eng.* **2015**, 17, 35–62.

(22) Lin, J.; Kim, D.; Tse, H. T.; Tseng, P.; Peng, L. L.; Dhar, M.; Karumbayaram, S.; Di Carlo, D. High-throughput physical phenotyping of cell differentiation. *Microsystems & Nanoengineering* **2017**, 3, 17013.

(23) Sajeesh, P.; Raj, A.; Doble, M.; Sen, A. K. Characterization and sorting of cells based on stiffness contrast in a microfluidic channel. *RSC Adv.* **2016**, 6 (78), 74704–74714.

(24) Hou, H. W.; Bhagat, A. A. S.; LinChong, A. G.; Mao, P.; Wei Tan, K. S.; Han, J. Y.; Lim, C. T. Deformability based cell margination-A simple microfluidic design for malaria-infected erythrocyte separation. *Lab Chip* **2010**, 10 (19), 2605–2613.

(25) Hur, S. C.; Henderson-MacLennan, N. K.; McCabe, E. R. B.; Di Carlo, D. Deformability-based cell classification and enrichment using inertial microfluidics. *Lab Chip* **2011**, 11 (5), 912–920.

(26) Huang, L. R.; Cox, E. C.; Austin, R. H.; Sturm, J. C. Continuous particle separation through deterministic lateral displacement. *Science* **2004**, 304 (5673), 987–990.

(27) Marin, B. C.; Ramirez, J.; Root, S. E.; Aklile, E.; Lipomi, D. J. Metallic nanoislands on graphene: A metamaterial for chemical, mechanical, optical, and biological applications. *Nanoscale Horiz* **2017**, 2 (6), 311–318.

(28) Amjadi, M.; Kyung, K. U.; Park, I.; Sitti, M. Stretchable, Skin-Mountable, and Wearable Strain Sensors and Their Potential Applications: A Review. *Adv. Funct. Mater.* **2016**, 26 (11), 1678–1698.

(29) Segev-Bar, M.; Haick, H. Flexible sensors based on nanoparticles. *ACS Nano* **2013**, 7 (10), 8366–78.

(30) Christov, I. C.; Cognet, V.; Shidhore, T. C.; Stone, H. A. Flow rate-pressure drop relation for deformable shallow microfluidic channels. *J. Fluid Mech.* **2018**, 841, 267–286.

(31) Raj, M. K.; DasGupta, S.; Chakraborty, S. Hydrodynamics in deformable microchannels. *Microfluid. Nanofluid.* **2017**, 21 (4), 70.

(32) Sneddon, I. N. The relation between load and penetration in the axisymmetric Boussinesq problem for a punch of arbitrary profile. *Int. J. Eng. Sci.* **1965**, 3 (1), 47–57.

(33) Wong, H.; Radke, C. J.; Morris, S. The motion of long bubbles in polygonal capillaries. Part 2. Drag, fluid pressure and fluid flow. *J. Fluid Mech.* **1995**, 292 (-1), 95.

(34) Fuerstman, M. J.; Lai, A.; Thurlow, M. E.; Shevkoplyas, S. S.; Stone, H. A.; Whitesides, G. M. The pressure drop along rectangular microchannels containing bubbles. *Lab Chip* **2007**, 7 (11), 1479–89.

(35) Bretherton, F. P. The Motion of Long Bubbles in Tubes. *J. Fluid Mech.* **1961**, 10 (2), 166–188.

(36) Yuya, P. A.; Patel, N. G. Analytical model for nanoscale viscoelastic properties characterization using dynamic nanoindentation. *Philos. Mag.* **2014**, 94 (22), 2505–2519.

(37) Daddi-Moussa-Ider, A.; Rallabandi, B.; Gekle, S.; Stone, H. A. A reciprocal theorem for the prediction of the normal force induced on a particle translating parallel to an elastic membrane. **2018**, arXiv:1804.08429. arXiv.org e-Print archive. <http://arxiv.org/abs/1804.08429> (accessed on May 24, 2018).

(38) Chen, C. L.; Mahalingam, D.; Osmulski, P.; Jadhav, R. R.; Wang, C. M.; Leach, R. J.; Chang, T. C.; Weitman, S. D.; Kumar, A. P.; Sun, L.; Gaczynska, M. E.; Thompson, I. M.; Huang, T. H. Single-cell analysis of circulating tumor cells identifies cumulative expression patterns of EMT-related genes in metastatic prostate cancer. *Prostate* **2013**, 73 (8), 813–26.